# Improved Stepped Frequency Microwave Radiometer Tropical Cyclone Surface Winds in Heavy Precipitation

BRADLEY W. KLOTZ

*Cooperative Institute for Marine and Atmospheric Studies, Rosenstiel School of Marine and Atmospheric Science, University of Miami, Miami, Florida*

ERIC W. UHLHORN

*NOAA/AOML/Hurricane Research Division, Miami, Florida*

## ABSTRACT

Surface wind speeds retrieved from airborne stepped frequency microwave radiometer (SFMR) brightness temperature measurements are important for estimating hurricane intensity. The SFMR performance is highly reliable at hurricane-force wind speeds, but accuracy is found to degrade at weaker wind speeds, particularly in heavy precipitation. Specifically, a significant overestimation of surface wind speeds is found in these conditions, suggesting inaccurate accounting for the impact of rain on the measured microwave brightness temperature. In this study, the wind speed bias is quantified over a broad range of operationally computed wind speeds and rain rates, based on a large sample of collocated SFMR wind retrievals and global positioning system dropwindsonde surface-adjusted wind speeds. The retrieval bias is addressed by developing a new SFMR C-band relationship between microwave absorption and rain rate ($\kappa - R$) from National Oceanic and Atmospheric Administration WP-3D aircraft tail Doppler radar reflectivity and in situ Droplet Measurement Technologies Precipitation Imaging Probe measurements to more accurately model precipitation impacts. Absorption is found to be a factor of 2 weaker than is estimated by the currently operational algorithm. With this new $\kappa–R$ relationship, surface wind retrieval bias is significantly reduced in the presence of rain at wind speeds weaker than hurricane force. At wind speeds greater than hurricane force where little bias exists, no significant change is found. Furthermore, maximum rain rates computed using the revised algorithm are around 50% greater than operational measurements, which is more consistent with maximum reflectivity-estimated rain rates in hurricanes.

## 1. Introduction

Aircraft reconnaissance and research missions are designed to observe a tropical cyclone (TC) to obtain the best representation of various storm-dependent features, including the surface wind speed (Gray et al. 1991; Aberson et al. 2006; Rogers et al. 2006, 2013). A fairly recent development for obtaining surface wind measurements is the installation of stepped frequency microwave radiometers (SFMRs; Uhlhorn and Black 2003; Uhlhorn et al. 2007) on all U.S. Air Force Reserve Command (AFRC) and National Oceanic and Atmospheric Administration (NOAA) hurricane-penetrating aircraft. The SFMR measures brightness temperatures ($T_b$) of the ocean surface and atmosphere at six C-band microwave channels (Swift et al. 1984), and an inversion algorithm is used to retrieve wind speed. When viewed at nadir, the apparent sea surface $T_b$ generally increases with surface foam coverage due to wave breaking (Nordberg et al. 1971; Rosenkranz and Staelin 1972). Since the increase in foam is correlated with surface wind speed (Ross and Cardone 1974; Webster et al. 1976; Swift et al. 1984; Tanner et al. 1987), $T_b$ increases with surface wind speed ($U_{sfc}$). Furthermore, the $T_b$ (or alternatively, the surface emissivity $\varepsilon$) sensitivity to wind speed is greatest at hurricane-force wind speeds (10 m $U_{sfc} > 33$ m s$^{-1}$) and is therefore particularly useful for measuring the strongest winds. However, sensitivity is high enough to overcome instrument noise limitations at surface wind speeds $> 5$ m s$^{-1}$.

At C band, microwave frequencies are far enough removed from the 22-GHz water vapor and 60-GHz oxygen

*Corresponding author address:* Bradley Klotz, CIMAS, Rosenstiel School of Marine and Atmospheric Science, University of Miami, 4600 Rickenbacker Causeway, Miami, FL 33149-1098.
E-mail: bklotz@rsmas.miami.edu

absorption bands that the intervening atmosphere is relatively transparent (Smith 1982). Also, radiative extinction by clouds is reasonably negligible below ~10 GHz (Tsang et al. 1977). However, large raindrops that are characteristic of tropical convective precipitation are a measureable absorber of radiation at C-band frequencies for rain rates exceeding ~3 mm h$^{-1}$ (Olsen et al. 1978). Precipitation generally results in an increase in the observed $T_b$. In contrast to the $T_b$ versus $U_{sfc}$ dependence, which is only weakly dependent on the microwave frequencies used, the $T_b$ (or, rain absorption coefficient) has a much stronger dependence on frequency in the presence of rain. Thus, multiple $T_b$ observations at closely spaced frequencies are needed to retrieve the wind speed under all conditions expected in hurricanes.

The current operational version of the SFMR $\varepsilon$ versus $U_{sfc}$ model function was developed mainly from observations in mature hurricanes primarily to measure the maximum wind as it pertains to estimating a storm's intensity (Uhlhorn et al. 2007). Therefore, general application to all tropical systems was not, until now, thoroughly tested, especially for wind speeds weaker than hurricane force. This has important operational implications for forecasters making decisions on system classifications, for example, when to declare that a tropical storm has intensified to hurricane status. Additionally, the installation of SFMRs on all AFRC WC-130J reconnaissance aircraft beginning in 2008 has resulted in a greatly expanded operational role for observing surface wind speeds of tropical disturbances at all stages of development. With the large increase in available observations, it became apparent that in certain conditions, particularly at weak-to-moderate wind speeds coupled with heavy precipitation, the SFMR-retrieved wind speed was typically higher than expected. To address this issue, a proposed Joint Hurricane Testbed (JHT; Rappaport et al. 2012; Ralph et al. 2013) project was funded in order 1) to quantify the apparent SFMR surface wind speed (high) bias over the full range of wind speeds and rain rates expected in tropical disturbances (from depressions through hurricanes); and 2) to analyze the currently implemented retrieval algorithm for accuracy; and 3) to recommend improvements for real-time operations, if necessary.

Calculating the SFMR microwave radiative energy budget mainly consists of properly accounting for two primary contributions to the observed $T_b$: the radiative emission by the sea surface and the radiative absorption by rain. To develop the currently operational $\varepsilon$ versus $U_{sfc}$ function, the contribution by rain to the $T_b$ was assumed to be known. A model for the absorption coefficient dependence on rain rate was developed from historical radar reflectivity observations (Atlas and Ulbrich 1977; Olsen et al. 1978; Jorgensen and Willis 1982, hereinafter JW82),

but its impact on surface wind accuracy was not specifically examined, which was partially due to limited data sample size. Jiang et al. (2006) evaluated SFMR-derived rain rates as compared to other remote sensing–based precipitation measurements for a small sample from Hurricanes Bonnie (1998) and Humberto (2001) and found that the SFMR tended to underestimate high rain rates and overestimate low rain rates. Recently, Walsh et al. (2014) compared SFMR rain rates with both Wide-Swath Scanning Radar Altimeter (WSRA) radar attenuation–derived and Next-Generation Weather Radar (NEXRAD) reflectivity-derived rain-rate data and essentially arrived at the same conclusion. Each of these studies suggests a need to examine the SFMR rain absorption function and its potential to degrade both surface wind speed and rain-rate retrieval accuracies.

The primary goal of this work is to demonstrate that improvements to SFMR TC surface wind speed retrieval quality will be possible by implementing a revised coupled wind–rain geophysical model function (GMF) that more accurately accounts for the microwave contribution from rain than does the current operational version. A comprehensive set of airborne data consisting of independent, in situ surface wind observations and precipitation measurements in hurricanes is used to rederive a set of model coefficients resulting in a more consistent microwave radiation budget and ultimately, more accurate wind speed measurements in all conditions. In addition, rain-rate retrieval accuracy is improved by virtue of the coupling.

This paper is organized as follows: in section 2, data used to both assess the wind speed bias and to derive a new set of model function coefficients are described. The wind speed bias over the full range of expected winds and rain rates is evaluated in section 3. Section 4 describes the methodology for developing the new model function, and section 5 contains an evaluation of surface wind speeds and rain rates using the revised algorithm relative to the measurements computed for operations. Finally, section 6 presents a summary and some concluding remarks.

## 2. Data

### a. SFMR

SFMR data are obtained from nearly 170 NOAA WP-3D aircraft missions between 1999 and 2012 and from over 200 AFRC WC-130J missions from 2010 to 2012, including flights during the 2010 Impact of Typhoons on the Ocean in the Pacific (ITOP) field experiment (D'Asaro et al. 2014). All SFMR-retrieved surface wind speeds and rain rates have been reprocessed using the operationally implemented algorithm (Uhlhorn et al. 2007) and are low-pass filtered to 10-s average values,

intended to represent a 1-min mean at a fixed location (Powell et al. 1991; Uhlhorn and Nolan 2012). Data are flagged as invalid if the input $T_b$ values are found to be noisy, as indicated by the root-mean-square error (RMSE) of the forward geophysical model fit to the $T_b$ observations. A similar quality-control procedure is also implemented for real-time operations.

### b. GPS dropwindsondes

Global positioning system (GPS) dropwindsonde (hereinafter "dropsonde"; Hock and Franklin 1999) $U_{sfc}$ are used to develop the operational SFMR emissivity versus $U_{sfc}$ GMF by correlating collocated observations (Uhlhorn et al. 2007). A sample of 160 quality-controlled paired observations is used for model function development, while another ~240 dropsondes are used for evaluation purposes, including validation of observations from an older SFMR instrument version. Following Franklin et al. (2003), the surface wind speed is estimated by adjusting the mean lowest 150-m-layer wind speed [the "WL150" wind speed coded in the World Meteorological Organization (WMO) TEMP DROP message] using a cubic polynomial function (Uhlhorn et al. 2007). The present study uses a greater-than-one order-of-magnitude-larger sample (>2700) of dropsonde-measured surface-adjusted wind speeds in TCs from 1999 to 2012 to both evaluate current SFMR accuracy and develop a revised $\varepsilon$ versus $U_{sfc}$ function.

### c. Precipitation

#### 1) WP-3D PIP

To obtain independent measurements of rain in TCs from the aircraft, in situ data from a Droplet Measurement Technologies Precipitation Imaging Probe (PIP) are used. This instrument has a particle resolution of 100 $\mu$m and has a droplet detection range up to 6200 $\mu$m with a sampling area of 16.12 $cm^2$, measuring along the flight track at a rate of 1 Hz (Black and Hallet 2012). Quality-controlled data from the PIP are obtained from 14 radial legs in two hurricanes [10 in Katrina (2005) and 4 in Earl (2010)]. These flights were chosen because of the reasonably high quality of PIP data (R. Black 2012, personal communication). The PIP rain-rate measurements are correlated with concurrent, collocated radar reflectivity data to develop a practical radar reflectivity ($Z$) versus PIP rain-rate ($R_{pip}$) relationship for computing radar rain estimates to address questions about SFMR rain absorption accuracy.

#### 2) WP-3D tail Doppler radar

A second independent estimate of rain used in this study is derived from NOAA tail Doppler radar (TDR)

reflectivity observations. Each NOAA WP-3D is equipped with a vertically scanning, X-band Doppler radar in the tail of the aircraft. The TDR is used primarily for three-dimensional mapping of the TC wind field (Jorgensen et al. 1983; Jorgensen 1984; Marks 1985; Marks et al. 1992), and implements a mechanical ±20° fore/aft scanning technique for retrieving horizontal wind vectors (Gamache et al. 1995). In this study, vertical profiles of TDR reflectivities are used to quantify precipitation below the freezing level along the flight track. These profiles have a vertical resolution of 150 m and an along-track resolution of 1.5 km (Lorsolo et al. 2010). In addition to reflectivity profiles obtained on the 14 radial legs coincident with the PIP observations, data from 26 radial legs in three different hurricanes [14 in Rita (2005), 5 in Felix (2007), 7 in Bill (2009)] are examined to quantify a relationship between the TDR reflectivity-derived rain rate and the increase in SFMR $T_b$ due to microwave absorption.

## 3. SFMR wind speed bias

The SFMR surface wind speed retrieval bias relative to surface-adjusted GPS dropsonde wind speeds is evaluated. The SFMR wind speed ($U_{sfmr}$) and rain rate ($R_{sfmr}$) is paired with the dropsonde-measured $U_{sfc}$ at the time of dropsonde launch. Despite the fact that a dropsonde at the surface is generally horizontally displaced from the launch location due to transport by the wind, most of the displacement is in the azimuthal direction with respect to the TC center, while the horizontal wind gradient is largest in the radial direction. As found by Uhlhorn et al. (2007), there is no statistical difference between using this approach of correlation versus pairing measurements at the same radial distance from the storm center.

These SFMR and dropsonde observations are placed into wind speed and rain-rate bins based on the SFMR measurements. The five wind speed bins range from tropical depression intensity or less ($U_{sfmr} < 17$ m s$^{-1}$), weak tropical storm ($17 \leq U_{sfmr} < 25$ m s$^{-1}$), strong tropical storm ($25 \leq U_{sfmr} < 33$ m s$^{-1}$), category 1 and 2 hurricanes ($33 \leq U_{sfmr} < 50$ m s$^{-1}$), and major categories 3 through 5 hurricanes ($U_{sfmr} \geq 50$ m s$^{-1}$), as defined somewhat arbitrarily by the Saffir–Simpson wind speed scale. Four rain-rate bins are divided equally every 10 mm h$^{-1}$ starting from zero up to rain rates of $R_{sfmr} > 30$ mm h$^{-1}$. Differences between SFMR- and dropsonde-measured wind speeds (i.e., $\delta U = U_{sfmr} - U_{sfc}$) are calculated along with their respective bin-average values.

Table 1 shows data sample sizes for each bin. Although there are numerous missions with available data, the vast majority of measurements are in weak precipitation

TABLE 1. Total number of SFMR and GPS dropsonde pairs for the designated SFMR-based wind speed and rain-rate bins (in $m\,s^{-1}$ and $mm\,h^{-1}$, respectively). Data included are from years 1999–2012. Observed dropsonde wind speed pairs are noted in parentheses with the difference between the total and observed data representing the number of synthetic pairs.

| | $0 \leq U_{sfmr} < 17$ | $17 \leq U_{sfmr} < 25$ | $25 \leq U_{sfmr} < 33$ | $33 \leq U_{sfmr} < 50$ | $U_{sfmr} \geq 50$ |
|---|---|---|---|---|---|
| $0 \leq R_{sfmr} < 10$ | 1356 (1356) | 690 (690) | 354 (354) | 196 (196) | 27 (27) |
| $10 \leq R_{sfmr} < 20$ | 54 (16) | 292 (73) | 290 (124) | 335 (134) | 25 (21) |
| $20 \leq R_{sfmr} < 30$ | 23 (5) | 96 (12) | 92 (44) | 144 (69) | 36 (24) |
| $R_{sfmr} \geq 30$ | 5 (1) | 19 (7) | 29 (18) | 89 (48) | 57 (23) |

($R_{sfmr} < 10\,mm\,h^{-1}$). Typically, reconnaissance and research missions do not specifically target areas of heavy rain outside of the TC eyewall for dropsonde deployment. From Table 1, fewer than 10 direct surface wind observations were identified in winds $U_{sfmr} < 25\,m\,s^{-1}$ and rain rates $R_{sfmr} > 30\,mm\,h^{-1}$. This presents a significant issue, since the primary goal of this research is to quantify and ultimately correct wind speed retrieval bias in heavy rain conditions, particularly for weaker wind speeds.

To address this systematic dropsonde undersampling of surface wind speeds at high rain rates, surface-adjusted wind speeds are estimated from flight-level winds. Observed dropsonde WL150 wind speeds ($U_{WL150}$) and corresponding flight-level wind speeds are obtained from several NOAA WP-3D flights in hurricanes during the 2010 and 2011 seasons. Data are restricted to being radially outward of twice the radius of maximum wind speed to reduce the negative impact of TC warm-core-induced eyewall tilt (Dunion et al. 2003) and are only included if the flight-level wind speed was measured within ±60 mb of the standard 700-mb level. A total of 537 $U_{WL150}$ wind speeds are correlated with the flight-level wind speed ($U_{FL}$), and a quadratic polynomial is fit to the data using a least squares regression:

$$U_{WL150} = 2.30 \times 10^{-2} U_{FL}^2 + 0.72 U_{FL} + 3.21, \quad (1)$$

where both $U_{WL150}$ and $U_{FL}$ are in meters per second.

Figure 1 shows a scatterplot of the $U_{FL}$ versus $U_{WL150}$ data and regression fit. There is reasonably good correlation ($r = 0.91$) with an RMSE of $5.4\,m\,s^{-1}$. The residual scatter around this relationship may be due to several potential factors, including both small-scale variability and low-wavenumber asymmetric structural differences between the surface and flight level (Uhlhorn et al. 2014). This is not unexpected, as Dunion et al. (2003) found a similar result comparing 700-mb flight-level winds to the lowest 500-m layer-mean dropsonde wind speed ($r = 0.82$; RMSE = $7.8\,m\,s^{-1}$). Although some additional error in the estimated surface wind speed will result from this relationship, such a penalty for obtaining surface wind measurements in strong precipitation appears necessary. Next, flight-level

winds are obtained from numerous aircraft missions over the 1999–2012 period in which the SFMR-retrieved rain rate exceeds $10\,mm\,h^{-1}$ but no corresponding dropsonde measurement is available. A synthetic surface wind speed is calculated by computing the $U_{WL150}$ estimate from the flight-level wind speed using Eq. (1) and then adjusting the surface similarly to actual dropsonde data. In Table 1, the number of synthetic pairs per bin is determined by subtracting the number of real observations (in parentheses) from the total number for each bin. The percentage of synthetic dropsonde $U_{sfc}$ estimates is largest for the high rain-rate bins and lower wind speeds bins where the number of direct observations is particularly lacking.

A random 80% sample of $\delta U$, $U_{sfmr}$, and $R_{sfmr}$ is drawn from each wind speed and rain-rate bin, including the synthetic data, to quantify the bias as a function of the SFMR wind/rain retrievals. Sample mean values and standard deviations for each bin are computed, and a polynomial is fit to the bin-averaged data using a
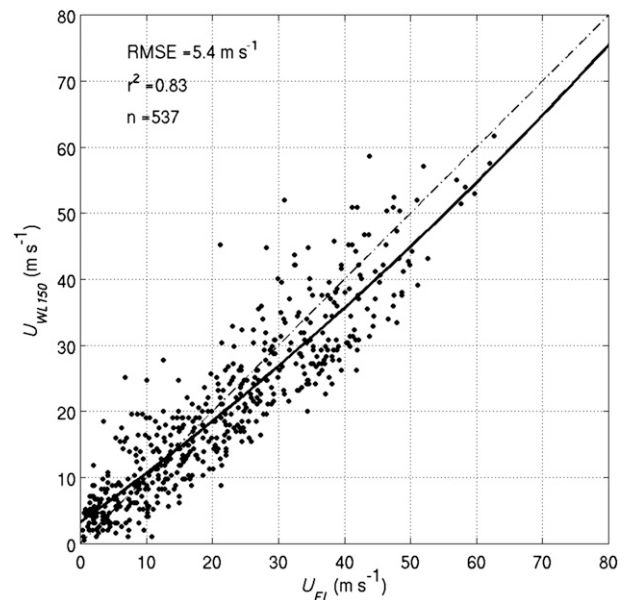


FIG. 1. Scatterplot of flight-level ($U_{FL}$) vs WL150 ($U_{WL150}$) dropsonde wind speed and the quadratic regression fit (solid line). The dashed–dotted line is the line of perfect correlation.
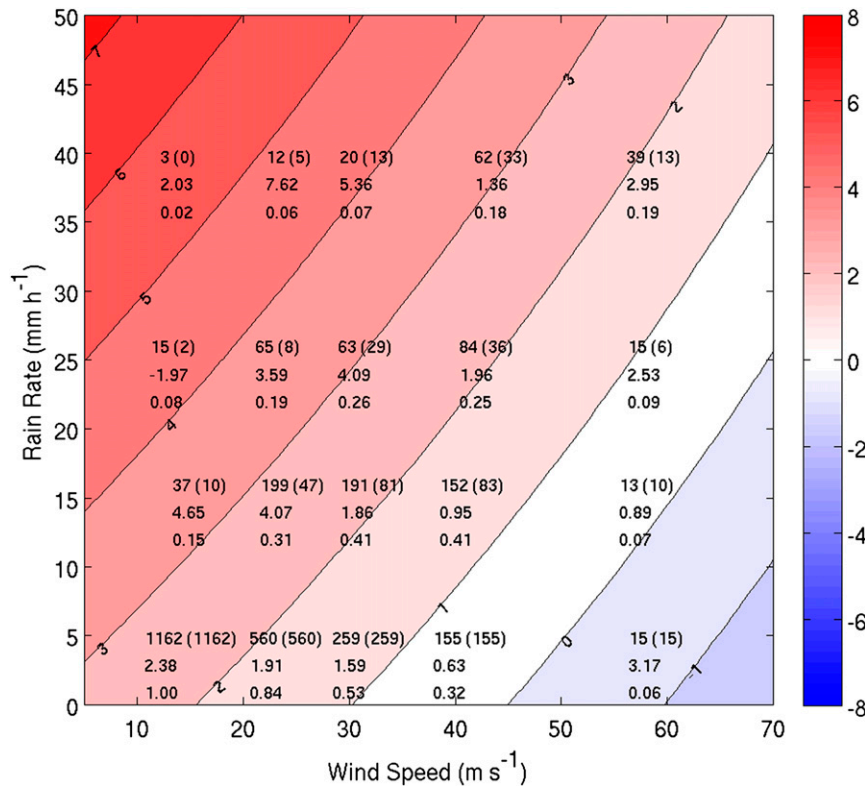
FIG. 2. SFMR wind speed bias-correction model [Eq. (2)] on the 80% random sample of SFMR–dropsonde pairs. Positive biases correspond with red colors, and negative biases correspond with blue colors. Text on the figure indicates the total number of pairs within the random sample (with real pairs in parentheses, similar to Table 1), the bin-mean wind speed bias, and the bin standard deviation weight applied during the model development.

weighted least squares regression. The applied weights are the inverse standard deviation for each bin multiplied by the minimum standard deviation over all bins. For example, the bin with the smallest standard deviation receives a weight of 1.0, and weights tend toward zero with increasing standard deviation. The resulting regression equation is

$$\delta U = -6.79 \times 10^{-2} U_{sfmr} + 9.36 \times 10^{-2} R_{sfmr}$$
$$- 3.90 \times 10^{-4} U_{sfmr} R_{sfmr} + 3.05, \qquad (2)$$

where $\delta U$ and $U_{sfmr}$ are in meters per second. Generally, the bias increases with rain rate and decreases with wind speed, as prior anecdotal evidence has suggested. Figure 2 graphically shows the bias ($\delta U$) as a function of $U_{sfmr}$ and $R_{sfmr}$ according to Eq. (2). Also shown in Fig. 2 are the sample sizes for each bin, mean biases, and the weight given to the particular bin for estimating the regression coefficients. The remaining 20% of the sample are used to obtain an independent estimate of the bias-correction model's uncertainty. The mean bias of the independent sample is $+2.2 \pm 0.3 \, \text{m s}^{-1}$ (95% confidence),

and after applying the adjustment in Eq. (2) to $U_{sfmr}$, the mean bias of the independent sample is a statistically insignificant $-0.1 \pm 0.3 \, \text{m s}^{-1}$.

The bias correction in Eq. (2) is currently being used by the National Hurricane Center for operational hurricane analysis when airborne reconnaissance data are available. Given $U_{sfmr}$ and $R_{sfmr}$ transmitted in the high-density observations (HDOB) messages, the bias $\delta U$ is computed and subtracted from $U_{sfmr}$ to obtain a more accurate SFMR wind speed. Later in this study, when deriving the rain absorption coefficient, this same correction will be applied to $U_{sfmr}$ to compute the surface emissivity contribution to the observed $T_b$.

## 4. Algorithm revisions

### a. Surface emissivity versus wind speed

In an earlier version of the SFMR wind speed retrieval algorithm used prior to 2006 (Uhlhorn and Black 2003), surface wind speed accuracy was validated from 10 to $50 \, \text{m s}^{-1}$. Observations in major hurricanes during the 2003–05 seasons indicated a lack of SFMR retrievals at

TABLE 2. Coefficients for the wind-induced emissivity vs wind speed model are provided for the operational algorithm and for the revised algorithm. For the revised version, the data are in conditions with no precipitation (i.e., rain rate $< 2 \, \text{mm h}^{-1}$).

| | $a_1$ | $a_2$ | $a_3$ | $a_4$ | $a_5$ | $a_6$ | $w_u$ |
|---|---|---|---|---|---|---|---|
| Operational | $4.012 \times 10^{-4}$ | $2.866 \times 10^{-3}$ | $-4.177 \times 10^{-4}$ | $5.849 \times 10^{-5}$ | $-5.666 \times 10^{-2}$ | $3.314 \times 10^{-3}$ | 31.9 |
| Revised | $1.232 \times 10^{-3}$ | $3.440 \times 10^{-3}$ | $2.492 \times 10^{-4}$ | $7.020 \times 10^{-5}$ | $-9.266 \times 10^{-2}$ | $5.444 \times 10^{-3}$ | 37.0 |

the expected category 4 and 5 maximum winds as compared to near-surface dropsonde measurements. To address this discrepancy, an emissivity versus wind speed ($\varepsilon - U_{sfc}$) model was developed based on a sample of 160 in situ dropsonde surface wind speeds (Uhlhorn et al. 2007), which corrected the systematic SFMR extreme wind speed ($U_{sfc} > 60 \, \text{m s}^{-1}$) underestimation.

Because of the relatively limited sample size from which the $\varepsilon - U_{sfc}$ relationship was developed, measurements in precipitating regions could not be excluded, and the impact of rain on brightness temperature was estimated to compute the SFMR surface emissivity. Implicit in the assumption of accurate emissivity values was that the rain absorption model was unbiased, at least to an acceptable level. With a vast increase in collocated SFMR and dropsonde wind speed observations since then, it has become clear that SFMR wind speeds are typically overestimated within weaker wind speed regimes coupled with heavy precipitation, and a biased rain absorption model is one possible explanation for this problem.

An evaluation of the currently implemented operational $\varepsilon - U_{sfc}$ model version is performed by reasonably eliminating wind observations in precipitation. A sample of dropsondes from over 200 NOAA and AFRC flights between 2005 and 2012 was used to compare with 10-s averaged SFMR-measured emissivity at the time of dropsonde launch. At lower dropsonde wind speeds of $U_{sfc} < 35 \, \text{m s}^{-1}$, measurements for which $R_{sfmr} < 2 \, \text{mm h}^{-1}$—which is near the noise level—are retained; for speeds $35 < U_{sfc} < 60 \, \text{m s}^{-1}$, only measurements with $R_{sfmr} < 10 \, \text{mm h}^{-1}$ are saved; however, all measurements for $U_{sfc} > 60 \, \text{m s}^{-1}$ are included, regardless of the rain rate, since the impact of rain at high wind speeds is far less than at lower wind speeds due to the high surface emissivity. After removing these observations, 1513 SFMR–dropsonde measurement pairs are retained over the wind speed range $0 < U_{sfc} < 75 \, \text{m s}^{-1}$.

The nadir-incidence surface emissivity is computed from the SFMR $T_b$ by rearranging the radiative transfer equation [Eq. (A6) of Uhlhorn and Black 2003]. In the absence of precipitation, it is possible to set $\tau_r = 1$ in Eq. (1) from Uhlhorn et al. (2007) to obtain the emissivity of the ocean surface:

$$\varepsilon = \frac{\tau_a^{-1}(T_b - T_{up}) - T_{sky}}{T_s - T_{sky}}, \quad (3)$$

where $T_b$ is the SFMR-measured brightness temperature, $T_{up}$ is the upwelling brightness temperature from the atmosphere below the aircraft, $T_{sky}$ is the downwelling total atmospheric brightness temperature plus cosmic background, $T_s$ is the sea surface temperature, and $\tau_a$ is the atmospheric transmissivity of the layer below the aircraft. The nadir-incidence Fresnel reflection coefficient ($\Gamma$) at frequency $f$ is calculated using the Klein and Swift (1977) algorithm for given $T_s$ and surface salinity ($S$), and the smooth surface emissivity is $\varepsilon_0 = 1 - \Gamma$. The nadir, wind-induced, excess emissivity ($\varepsilon_w$) is obtained by subtracting $\varepsilon_0$ from the measured surface emissivity:

$$\varepsilon_w(f, U_{sfc}) = \varepsilon(f, T_s, S, U_{sfc}) - \varepsilon_0(f, T_s, S). \quad (4)$$

The GMF directly relates $\varepsilon_w$ and $U_{sfc}$ at each SFMR frequency channel. Because it is the lowest frequency (longest wavelength), measurements from the 4.74-GHz channel are expected to be the least impacted by rain, and this channel is therefore chosen as the reference for the $\varepsilon_w - U_{sfc}$ model. A functional form identical to the operational model consisting of two linear functions connected at intermediate wind speeds with a quadratic function [Eq. (5)] is fit to the observations with a constrained piecewise regression using a Levenberg–Marquardt method:

$$\varepsilon_{w,4.74} = \begin{cases} a_1 U_{sfc} & 0 \leq U_{sfc} < w_l \\ a_2 + a_3 U_{sfc} + a_4 U_{sfc}^2 & w_l \leq U_{sfc} < w_u \\ a_5 + a_6 U_{sfc} & w_u \leq U_{sfc} \end{cases}. \quad (5)$$

As in Uhlhorn et al. 2007, the low-wind breakpoint is set to $w_l = 7 \, \text{m s}^{-1}$, where wave breaking and foam begins to occur (Monahan 1971; Ross and Cardone 1974), and the high-wind breakpoint $w_u = 37.0 \, \text{m s}^{-1}$ is determined via trial and error to minimize the RMSE of the fit. Revised coefficients for the model function are given in Table 2 for the 4.74-GHz channel.

Figure 3a shows $\varepsilon_{w,4.74}$ versus $U_{sfc}$, along with the operational and revised models at 4.74 GHz. The operational version developed from the relatively limited data sample (Uhlhorn et al. 2007) appears remarkably accurate in comparison to the function determined here based on the much larger sample size. The RMSE of the fit is 0.012 (or, in dimensional terms, ~3.5 K at
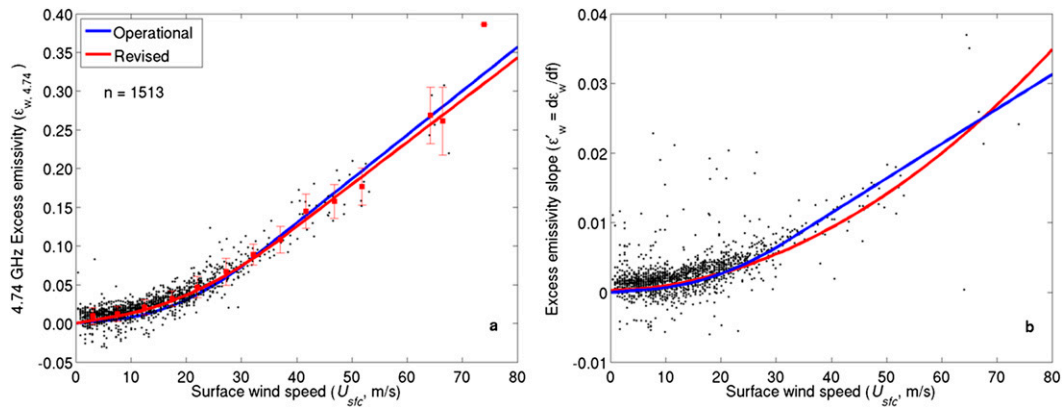
FIG. 3. Scatterplots of (a) wind-induced excess emissivity ($\varepsilon_w$) at 4.74 GHz as a function of the surface-adjusted dropsonde wind speed ($U_{sfc}$), and (b) excess emissivity slope with respect to frequency ($\varepsilon'_w = d\varepsilon_w/df$) vs $U_{sfc}$. Blue (red) lines are operationally implemented (revised) model functions. In (a), wind speed bin-averaged $\varepsilon_w$ is plotted as red markers, with bin standard deviations indicated by error bars.

$T_s = 301$ K), which is nearly equivalent to the emissivity residual error in the operational version. Although the difference is quite small, the most significant difference is found in the $10–20\,\mathrm{m\,s^{-1}}$ range, where the revised emissivity values are on average slightly higher.

In addition, there is a small frequency-dependent component of the excess emissivity that must be considered. The assumed frequency sensitivity ($\varepsilon'_w = d\varepsilon_w/df$) was based on historical passive microwave observations of the sea surface (Webster et al. 1976), but until now it has not been verified with SFMR data. The operational algorithm version's excess emissivity sensitivity to frequency is $\varepsilon'_w = 0.15\varepsilon_w$, and therefore is wind speed–dependent via $\varepsilon_w$. To verify the validity of this frequency dependence, the slope $\varepsilon'_w$ is computed by fitting a least squares regression line to each set of the six $\varepsilon_w$ versus $f$ measurements. The resulting slope is then plotted as a function of $U_{sfc}$ (Fig. 3b). A quadratic polynomial is next fit to the observations:

$$\varepsilon'_w = 5.166 \times 10^{-6} U^2_{sfc} + 1.860 \times 10^{-5} U_{sfc} + 2.788 \times 10^{-4}. \tag{6}$$

The unit for $\varepsilon'_w$ is inverse gigahertz. The functional fit [Eq. (6)] and the slope function implemented in the operational algorithm are also plotted in Fig. 3b. Evidently, the small frequency dependence is currently estimated with a high degree of accuracy, since both the curves in Fig. 3b are reasonably close to each other, but this revised slope function is chosen and implemented as part of the proposed model function update to maintain consistency with the observations. The proposed revised GMF for emissivity applicable to all SFMR channels now reads

$$\varepsilon = \varepsilon_{w,4.74} + \varepsilon'_w \Delta f + \varepsilon_0, \tag{7}$$

where $\varepsilon_{w,4.74}$ and $\varepsilon'_w$ are functions of $U_{sfc}$, and $\Delta f = f - 4.74$ GHz.

### b. Microwave absorption by rain

The impact of precipitation on brightness temperature is generally represented by an attenuation coefficient, which is nominally a function of liquid water content, frequency, and temperature (e.g., Matrosov et al. 2002, 2005). At the low microwave frequencies of the SFMR, scattering may be neglected because of the large wavelength to dropsize ratio, even for large drops in tropical convection, and attenuation may be more simply represented by an absorption coefficient ($\kappa$). Also, the relatively small temperature variation in a TC may be safely neglected (Jiang et al. 2006). Development of the currently operational absorption versus rain-rate ($\kappa - R$) relationship (Uhlhorn and Black 2003) was primarily based on radar reflectivity-derived rain rates computed by JW82 in hurricane conditions.

#### 1) RAIN COLUMN DEPTH

SFMR rain-rate retrievals were examined in relation to other sources of precipitation observations (Jiang et al. 2006), and results of an intercomparison with radar-derived rain rates indicated a tendency for overestimating weak rain rates and underestimating strong rain rates. It was concluded that a possible cause for this apparent behavior was uncertainty in estimating the height of the rain column. In the operational implementation, the height of the rain column (i.e., the freezing level) is set to a constant 4 km above the surface. In the present calculations of the absorption coefficient, the freezing level ($H$) is estimated from the aircraft flight-level temperature and altitude assuming a typical hurricane temperature profile:
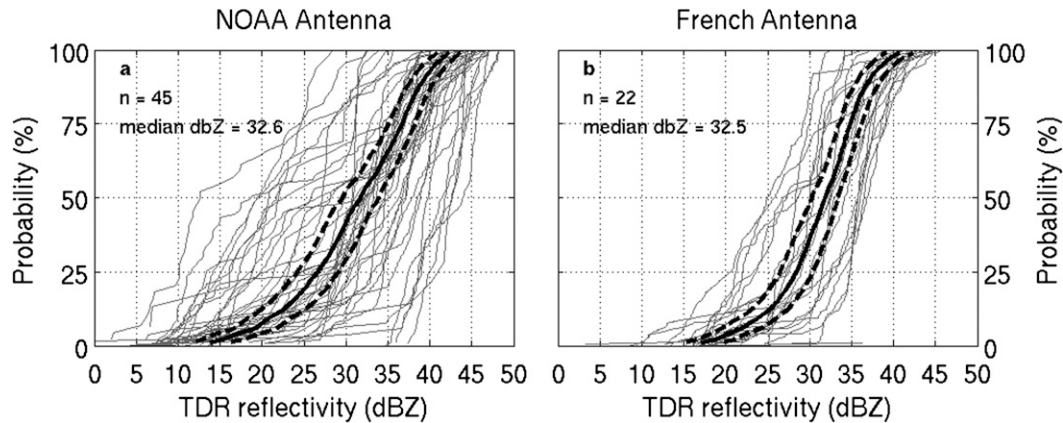
FIG. 4. Empirical cumulative distributions of layer-mean TDR reflectivity factor (dB$Z$) below the freezing level for (a) the NOAA parabolic antenna and (b) the French dual-flat-plate antenna. Each distribution is a radial leg: (a) 45 radial legs and (b) 22 radial legs. The solid black line in each panel is the composite mean cumulative distribution, with ±1 standard deviation (dashed lines).

$$H = h + \gamma^{-1} T_{\mathrm{amb}}, \qquad (8)$$

where $h$ is the aircraft altitude (m), $T_{\mathrm{amb}}$ is the ambient flight-level temperature (K), and $\gamma = 5.22 \times 10^{-3}\,\mathrm{K\,m^{-1}}$ is the mean lapse rate determined from a large number of dropsonde temperature profiles obtained in hurricanes (Zhang and Uhlhorn 2012).

### 2) TDR-DERIVED RAIN RATE IN HURRICANES

The JW82 reflectivity versus rain rate ($Z$–$R$) relationship is $Z = 300R^{1.35}$, where $R$ is in millimeters per hour and $Z$ is in $\mathrm{mm^6\,m^{-3}}$. With more data resources available, along with significant improvements to instrumentation, we revisit this relationship in light of the SFMR rain-rate retrievals. Specifically, path-averaged TDR reflectivity data are compared with in situ PIP rain-rate data obtained in several recent aircraft missions in TCs.

Since the primary purpose of the WP-3D TDR is for measuring wind, an accurate calibration of reflectivity has often been neglected. Jiang et al. (2006) review several assessments of radar reflectivity bias, which has previously been found to be between 5 and 8 dB too low. Jiang et al. (2006) compared TDR reflectivity with calibrated National Aeronautics and Space Administration ER-2 aircraft Doppler (EDOP) radar data and concluded that a 6-dB offset added to the TDR data produced acceptable (within ~1–2-dB error) reflectivity values. The currently accepted ad hoc approach to correct the apparent underestimation is to add 7 dB to the measured reflectivity factor (J. Gamache 2014, personal communication). Additionally, the radar antennas used on the two aircraft are not identical. One radar uses

a parabolic antenna ("NOAA antenna"), while the other uses a dual-flat-plate antenna ("French antenna"; Gamache et al. 1995). Because data from both radars are used, it is possible that calibration differences could impact results. To evaluate how well these radars were calibrated and how they relate to one another, a quantitative comparison of reflectivity cumulative distributions for each antenna reveals no major differences in measured reflectivity (Fig. 4). The median reflectivity computed from the composite cumulative distributions for both radars are nearly identical. Reflectivity from the NOAA antenna (Fig. 4a) appears to have a broader low rain-rate tail, suggesting greater sensitivity. The SFMR is not sensitive to such low rain-rates characteristic of weak, stratiform precipitation, and these low reflectivity data should not impact the overall SFMR results.

Layer-mean TDR reflectivity values vertically averaged from just above the sea surface (to eliminate sea clutter) to near the freezing level are computed for 14 radial profiles from two hurricanes (see section 2c). The bright band, which due to melting precipitation can increase the reflectivity by as much as 7 dB near the 0°C isotherm (Rinehart 2004), is removed by neglecting measurements within ~500 m of the estimated freezing level. Also, X-band TDR reflectivity is subject to significant rain attenuation over extended distances. However, at X-band frequencies the specific attenuation is ~0.2 dB km$^{-1}$ for reflectivity factor <40 dB$Z$, increasing to ~1 dB km$^{-1}$ at 50 dB$Z$ (e.g., Park et al. 2005). Since the range for the vertical profiles is at most ~3 km, an attenuation correction can be reasonably ignored here.

As an example, a radial distance/height TDR reflectivity vertical cross section from a single outbound radial leg in Hurricane Earl (2010) is shown in Fig. 5a. For this same radial leg, the below-freezing-level layer-mean
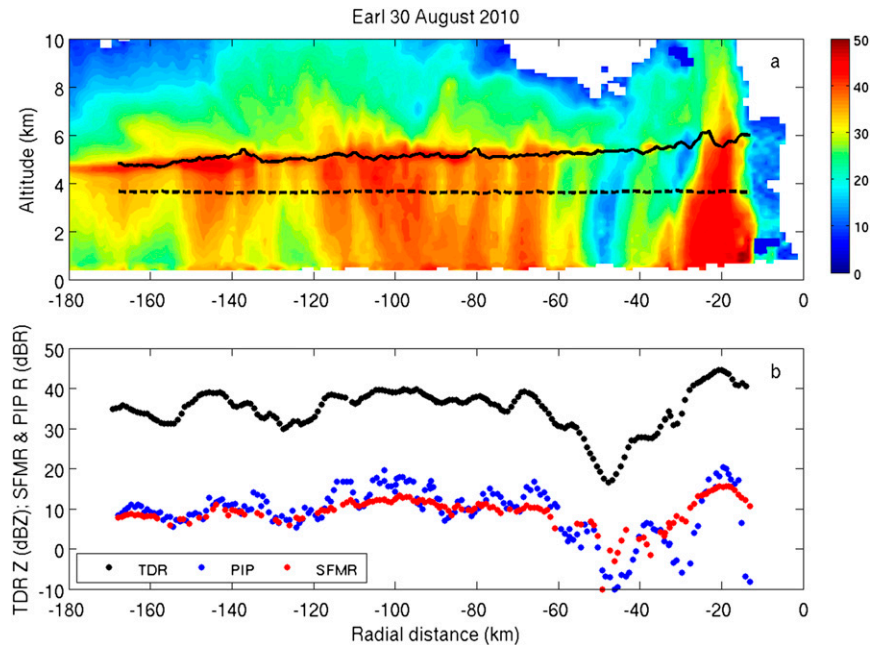
FIG. 5. (a) Tail Doppler radar reflectivity factor vertical cross section for a single outbound radial leg in Hurricane Earl (2010), and (b) rain column-average TDR reflectivity factor (black, dB$Z$), PIP in situ rain-rate factor (blue, dB$R_{\mathrm{pip}}$), and SFMR-retrieved rain-rate factor (red, dB$R_{\mathrm{sfmr}}$). In (a), the solid black line is the estimated freezing level and the dashed line is the aircraft flight altitude. Note that radar reflectivities near the bright band are removed from the layer averaging.

TDR reflectivity computed from the cross section, the in situ PIP rain rate, and the retrieved SFMR rain rate are shown in Fig. 5b. Qualitatively, all three independent measurements of the precipitation compare well, as the eyewall, outer rainbands, and relatively dry "moat" region are clearly identifiable. Peak layer-mean reflectivity in the eyewall around 20 km from the storm center is ~45 dB$Z$, consistent with maximum Tropical Rainfall

Measuring Mission Precipitation Radar reflectivity below the melting level (Jiang et al. 2013) in TCs. This reflectivity peak is collocated with a maximum SFMR rain rate of ~17 dB$R$ (or ~50 mm h$^{-1}$), and a peak PIP rain rate of ~21 dB$R$ (~125 mm h$^{-1}$). Notice in Fig. 5b that the variance in the in situ PIP rain rates is substantially higher than both the radar and SFMR data because of the much smaller sampling volume of the PIP. The SFMR
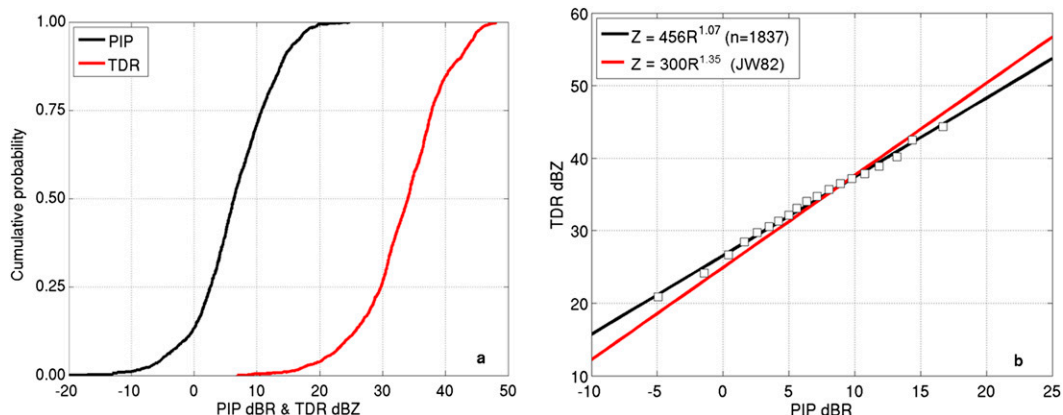


FIG. 6. (a) Empirical cumulative distributions are provided for the PIP rain-rate factor (black) and TDR column-mean reflectivity factor (red) for all samples ($n = 1836$) from the 14 matched radial legs, and (b) probability-matched PIP rain-rate factor vs TDR reflectivity with marks from 5% to 95% probability level are shown. In (b) the regression fit (black solid line) is provided, and the JW82 $Z$–$R$ hurricane relationship is plotted (red solid line).
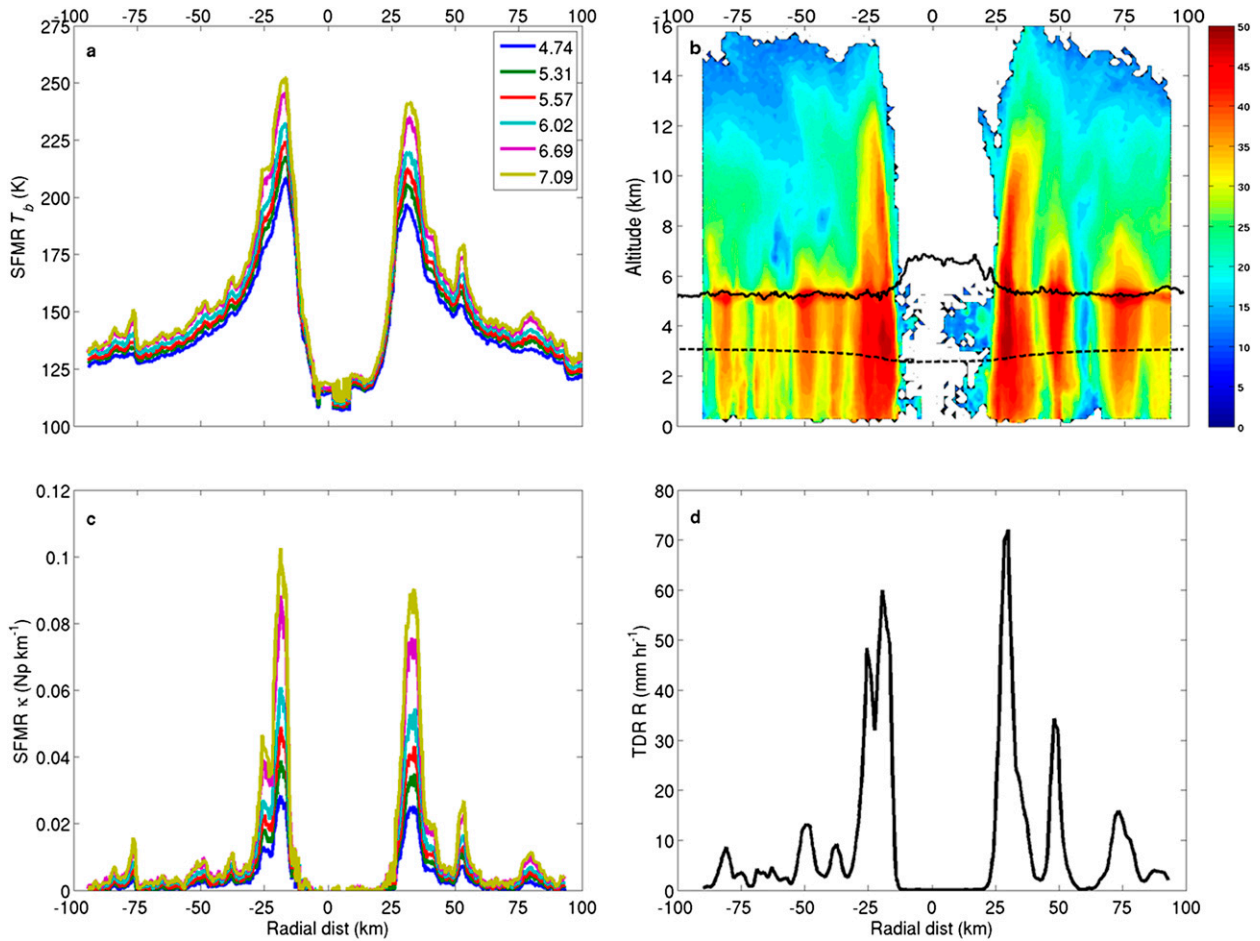
FIG. 7. Coordinated SFMR and TDR measurements for two radial passes (inbound and outbound from the center) in Hurricane Rita between 1506 and 1536 UTC 21 Sep 2005. The contents of the four panels are (a) SFMR $T_b$ (K) for all frequency channels, (b) vertical cross section of TDR reflectivity factor (dB$Z$), (c) SFMR-derived rain absorption coefficient ($\kappa$, Np km$^{-1}$), and (d) TDR layer-mean reflectivity-derived rain rate ($R_{tdr}$, mm h$^{-1}$). The solid and dashed lines in (b) indicate the estimated freezing level and the aircraft flight altitude, respectively.

and TDR have reasonably comparable sampling volumes and resulting data variability.

From the 14 aircraft radial legs, a sample of 1836 of collocated TDR reflectivity ($Z_{tdr}$) and PIP rain-rate ($R_{pip}$) data is obtained. Data are discarded when $Z_{tdr} < 7$ dB$Z$ or when the PIP number concentration is <200 drops per liter, since ultimately the C-band SFMR is insensitive to such weak precipitation. Cumulative distributions of TDR and PIP observations are shown in Fig. 6a. Median reflectivity and rain rate are ~33 dB$Z$ and ~6 dB$R$ (~3 mm h$^{-1}$), respectively. Variances for each quantity are reasonably comparable, although the PIP shows a larger weak precipitation tail. Maximum reflectivity in this sample is ~49 dB$Z$. Peak PIP rain rates are ~25 dB$R$ (~316 mm h$^{-1}$), although such extreme values are highly infrequent and would likely not be detected by the SFMR because of its far larger sampling volume.

To estimate a practical $Z$–$R$ relationship, statistical probability matching (Rosenfeld et al. 1993, 1994) is used, in which observations at specified percentile levels for each dataset are correlated. Probability levels are computed from 5% to 95% (Fig. 6b); the highest and lowest 5% are not considered because the radar (and its relatively large sampling volume) cannot resolve these highly localized extrema. Probability levels of PIP rain rate versus TDR reflectivity are shown on a log scale in Fig. 6b. A fit to these data results in the following $Z$–$R$ relationship:

TABLE 3. Empirically determined coefficients for Eq. (12) for the operational (top row) and updated (bottom row) versions of the $\kappa$–$R$ relationship.

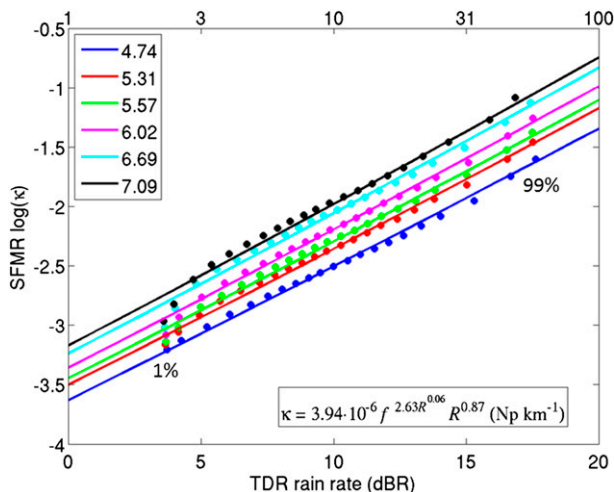| | $g$ | $c$ | $d$ | $b$ |
|---|---|---|---|---|
| Operational | $1.87 \times 10^{-6}$ | 2.60 | 0.0736 | 1.15 |
| Revised | $3.94 \times 10^{-6}$ | 2.63 | 0.0600 | 0.87 |

FIG. 8. Quantile–quantile plot of probability-matched TDR-derived rain-rate factor (dB$R_{tdr}$) vs SFMR-derived absorption coefficient [log($\kappa$)] for data (over 21 000 samples) obtained from 26 radial legs, and regression fit to data (solid lines), given by the empirical $\kappa$–$R$ relation in the figure. The corresponding linear rain rate is marked on the top horizontal axis. Probability levels are marked from 1%, 5%–95%, and 99%, with the lowest and highest 1% of the data annotated. Note the loss of SFMR sensitivity at the weakest rain rates, as there is much less change in absorption across the frequency band than at higher rain rates.

$$Z = 456R_{pip}^{1.07}. \tag{9}$$

For comparison, the JW82 hurricane $Z$–$R$ relationship is also shown in Fig. 6b. Each function yields a similar reflectivity value for the median rain rate, but the results here suggest a weaker radar sensitivity to rain rate than indicated by the JW82 results (i.e., a smaller rain-rate

exponent). Some of this apparent sensitivity loss may be due to the vertical averaging and inherent smoothing of the reflectivity data because the JW82 results were derived from a more direct point-by-point intercomparison of observations. Because of this vertical averaging, this $Z$–$R$ relationship in Eq. (9) should not be used for pointwise studies. An evaluation of the flight-level TDR reflectivity as compared to the layer-mean reflectivity finds a mean absolute difference on the order of ~1–1.5 dB. Such a small difference in reflectivity does not warrant the need to use the flight-level point measurement. In fact, the layer-mean value is more representative of the path-averaged microwave brightness temperatures observed by the SFMR, to which radar-derived rain rates are correlated for this study.

### 3) SFMR ABSORPTION VERSUS TDR RAIN RATE

The microwave rain absorption coefficient ($\kappa$) is computed by first solving for the total rain column transmissivity ($\tau_r$) in the SFMR radiative transfer equation:

$$c_2(1 - \varepsilon)\tau_r^{(1+h/H)} + c_1\tau_r^{h/H} + c_0 = 0, \tag{10}$$

where

$$c_2 = \tau_{a,h}[\langle T_{a,h}\rangle - \tau_{a,\infty}(\langle T_{a,\infty}\rangle + \langle T_{r,H}\rangle - T_c)],$$
$$c_1 = \tau_{a,h}[\varepsilon T_s + \tau_{a,\infty}(1 - \varepsilon)\langle T_{r,H}\rangle - \langle T_{a,h}\rangle - \langle T_{r,H}\rangle] + \langle T_{a,h}\rangle,$$
$$c_0 = \tau_{a,h}\langle T_{r,H}\rangle - T_b,$$

and $h/H \leq 1$, since absorption by frozen precipitation is neglected. In the coefficients for Eq. (10), the first subscript $a$ refers to atmospheric contribution, or $r$ for rain contribution; and the second subscript is either $h$ for
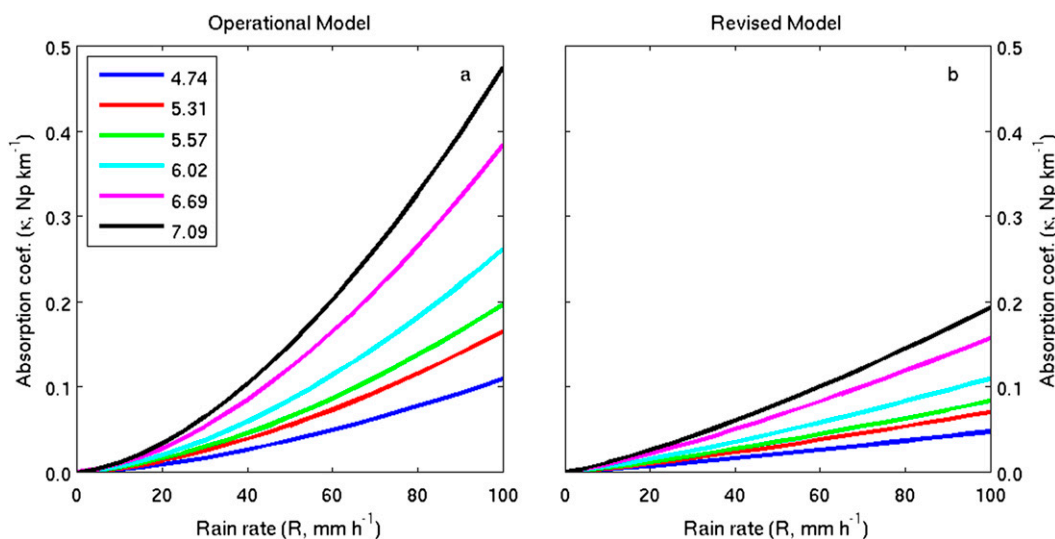


FIG. 9. (a) Currently operational and (b) revised rain absorption coefficient ($\kappa$, Np km$^{-1}$) model functions for each SFMR frequency channel.
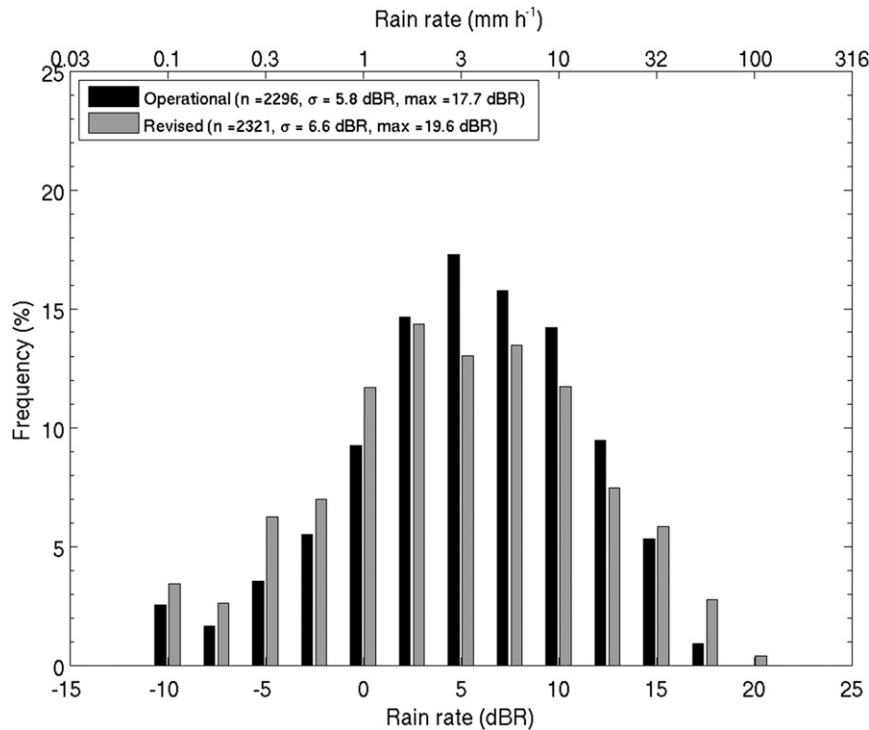
FIG. 10. Histograms for the operationally computed rain rates (black) and recomputed rain rates from the revised model (gray) for measurements that are paired with a dropsonde (not shown). Rain-rate factor (dB$R_{sfmr}$) is labeled at the bottom and corresponding linear rain rate ($R_{sfmr}$, mm h$^{-1}$) is labeled at the top of horizontal axis. Both a broader distribution and higher peak rain rates are obtained when using the revised model function. The maximum retrieved SFMR rain rate increases by nearly 2 dB$R$, or from 59 up to 91 mm h$^{-1}$.

contribution below the aircraft height, $H$ for total rain column contribution, or $\infty$ for total atmospheric contribution. Angle brackets denote a mass-weighted layer average physical temperature.

Collocated SFMR $T_b$ data and TDR reflectivity vertical profiles are obtained from 26 radial legs in three hurricanes (see section 2c). Because these data are independent of the coincident PIP dataset, a larger and more representative sample of the SFMR and TDR comparison is obtained for the development of the $\kappa$–$R$ function. The surface emissivity here is computed from the bias-corrected [Eq. (2)] operational SFMR-retrieved wind speed using the updated form of $\varepsilon_w$ from Eq. (7), and the flight-level temperature and altitude are used to compute the other quantities (i.e., column mean physical temperatures, gas transmissivity) to determine the coefficients $c_i$. Equation (10) is solved for $\tau_r$ using an iterative Newton–Raphson method, and the absorption coefficient is ly computed as

$$\kappa = -H^{-1} \ln(\tau_r). \qquad (11)$$

Layer-averaged TDR-derived rain rate ($R_{tdr}$) at the SFMR observation location is calculated using the $Z$–$R$

relationship [Eq. (9)]. Over 21 000 samples of $\kappa$ at each channel are paired with the collocated $R_{tdr}$ observations. For example, SFMR $T_b$ and TDR reflectivity, along with derived $\kappa$ and $R_{tdr}$, are shown in Fig. 7 for a complete radial traverse through Hurricane Rita between 1506 and 1536 UTC 21 September 2005. The $T_b$ (Fig. 7a) generally increases as the eyewall is approached because of the high-wind-induced surface emissivity. However, it is the spreading across the SFMR frequency channels that results in increased absorption (Fig. 7c). Clearly, this is highly correlated with the radar-derived rain rate (Fig. 7d).

An empirical $\kappa$–$R$ relationship is determined assuming a power law of the form $\kappa = aR_{tdr}^b$ consistent with the operational SFMR model for rain absorption. As in Olsen et al. (1978), the coefficient $a$ depends on frequency and rain rate and therefore the model can be written as

$$\kappa = g f^n R_{tdr}^b. \qquad (12)$$

The frequency exponent $n$ has been shown to have a small dependence on $R$ and is also expressed as a power law: $n = cR^d$ (Atlas and Ulbrich 1977). The empirical coefficients $b$, $c$, $d$, and $g$ are determined by
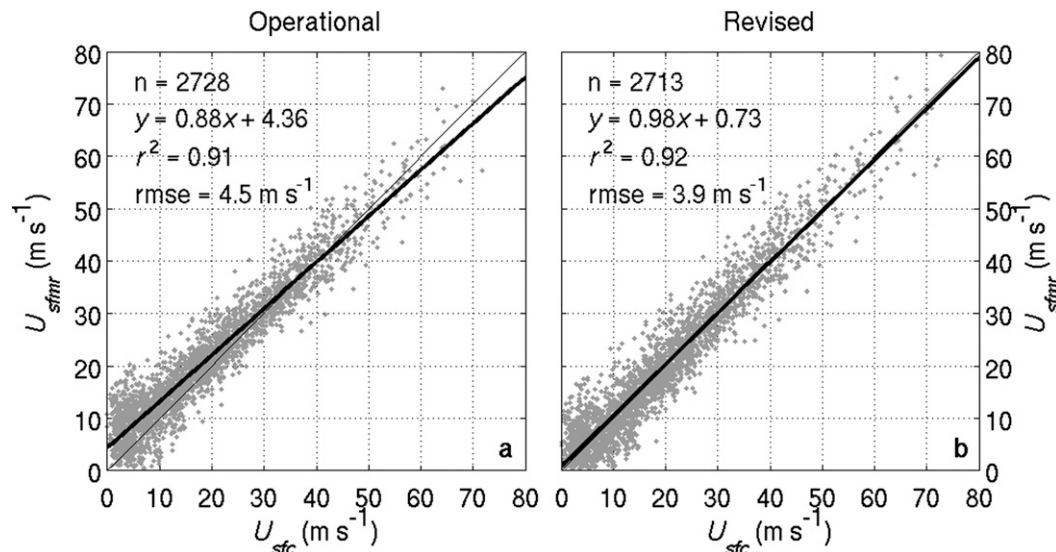
FIG. 11. (a) Scatterplot of dropsonde $U_{sfc}$ vs $U_{sfmr}$ for the operationally computed winds. (b) As in (a), but computed with the revised model function (gray points). Linear regression fits (thick black lines) and regression statistics are shown in each panel. Perfect correlation (thin gray line) is shown for reference.

fitting the SFMR absorption coefficient data to the TDR-derived rain-rate estimates. Cumulative probability levels from 1% to 99% are matched, and a Levenberg–Marquart nonlinear least squares method is used to fit Eq. (12) to the probability-matched data.

Coefficients for the currently operational version of the rain absorption model and the revised coefficients are given in Table 3. Figure 8 shows the data and regression fits for the revised version. Below ~5 dB$R$ (~3 mm h$^{-1}$), which corresponds to ~30 dB$Z$, the signal appears to be lost, indicating a lower limit of SFMR sensitivity. Note, also, that the real-time reporting precision for SFMR rain rate is 1 mm h$^{-1}$; retrieved values less than 0.5 mm h$^{-1}$ are reported as zero (or missing) rain rate. The highest 1% of TDR rain rates is $R_{tdr} > 55$ mm h$^{-1}$, whereas operationally measured SFMR rain rates rarely exceed this value. In Fig. 9, a comparison of the currently operational and revised $\kappa$–$R$ relationships suggests that the absorption is overestimated by roughly a factor of 2 across the frequency band. Thus, for a given set of $T_b$ observations, the operational algorithm would tend to assign too much of the brightness (and hence, rain) to the absorption and therefore too little to the emissivity (and hence, wind).

## 5. Evaluation

### a. Revised SFMR rain rates

As a consequence of the biased operational rain absorption model function, the dynamic range of retrieved rain rates was limited. Maximum rain rates rarely exceeded 55 mm h$^{-1}$, which is fairly low compared to in situ observed rain-rate values, even after accounting for spatial sampling mismatches between in situ and remote sensing observational estimates. This is a result mainly from an improper model sensitivity loss (i.e., small $dR/d\kappa$) at high rain rates. As indicated in Fig. 9a for the operational algorithm at high rain rates, a large increase in $\kappa$ results in only a small relative increase in the retrieved $R$, while in Fig. 9b, a similar increase in $\kappa$ will yield a much larger increase in $R$.

SFMR rain rates are computed using both the operational algorithm and proposed modifications for the sample collocated with dropsonde surface winds, and distributions are shown in Fig. 10. Overall, the proposed new absorption model increases the variance of SFMR-retrieved rain rates and yields far greater maximum values, up to $R_{sfmr} = 91$ mm h$^{-1}$ in this sample, as compared to 59 mm h$^{-1}$ in the operational retrievals. Recently, SFMR rain rates have been evaluated against rain rates derived from airborne WSRA radar attenuation measurements, as well as coastal WSR-88D NEXRAD reflectivity-derived values (Walsh et al. 2014). Based on extensive observations in Hurricane Irene (2011) offshore of the North Carolina Outer Banks, SFMR rain rates were found to be biased low at high rain rates, and biased high at low rain rates, consistent with the conclusions of Jiang et al. (2006) and the results found in this work.

### b. Revised SFMR surface wind speeds

SFMR wind speeds are recomputed using the revised algorithm, and the improvement in retrieval
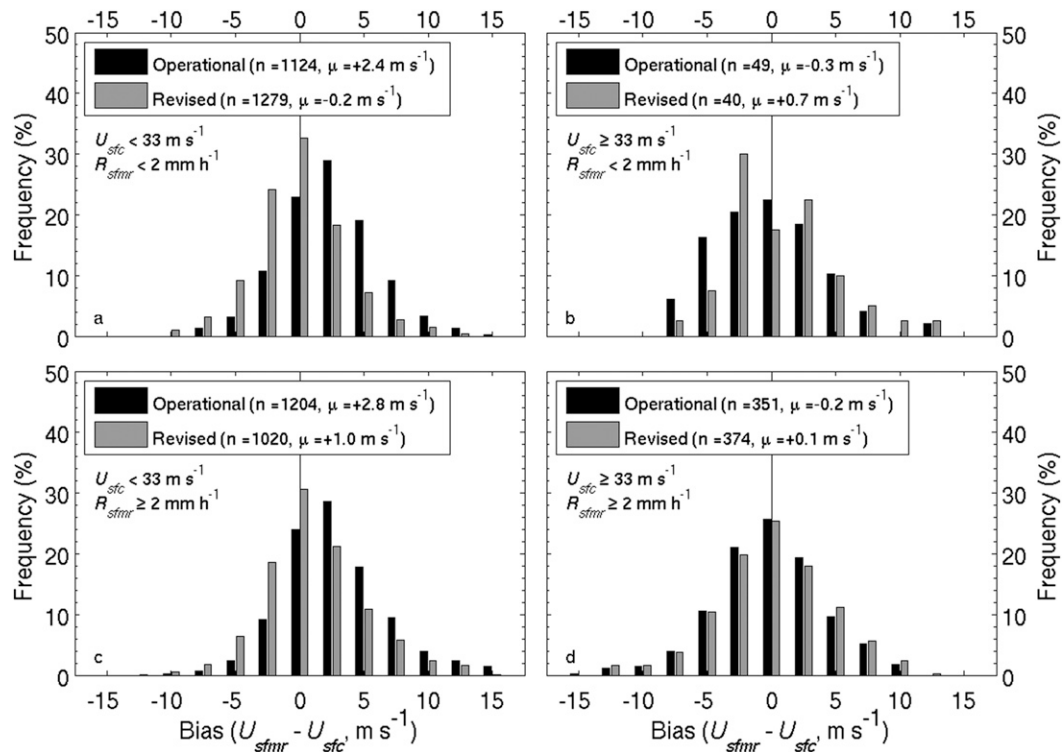
FIG. 12. Histograms of the operational (black) and revised (gray) wind speed bias ($U_{sfmr} - U_{sfc}$, m s$^{-1}$) for (a),(c) speeds less than ($U_{sfc} < 33$ m s$^{-1}$) and (b),(d) greater than ($U_{sfc} \geq 33$ m s$^{-1}$) the minimum hurricane threshold in (a),(b) nonprecipitating conditions ($R_{sfmr} < 2$ mm h$^{-1}$) and in (c),(d) precipitating conditions ($R_{sfmr} \geq 2$ mm h$^{-1}$). Sample sizes and mean biases for each group are indicated.

accuracy over the operationally determined speeds is evaluated against the collocated observed dropsonde surface wind speed measurements. Figure 11 shows scatterplots for wind speeds computed using the operational algorithm and the proposed revised algorithm. A significant improvement in surface wind speed accuracy is found over all sampled wind speeds and rain rates based on the correlation (slope of best-fit line increases from 0.88 to 0.98), while the RMSE decreases from 4.5 to 3.9 m s$^{-1}$. Note that the sample sizes are slightly different, since the numerical inversion procedure does not guarantee solutions for all measurements.

Further details about surface wind speed retrieval improvements are examined by stratifying according to wind speed greater than and less than the hurricane wind speed threshold ($U_{sfc} = 33$ m s$^{-1}$), and whether the measurement is inside or outside of precipitation. A rain/no-rain threshold of $R_{sfmr} = 2$ mm h$^{-1}$ is chosen, since the SFMR is not sensitive at these weak rain rates. Figure 12 shows frequency histograms of SFMR wind speed bias, defined as the difference between the SFMR-retrieved wind speed and the collocated dropsonde-measured surface wind speed ($U_{sfmr} - U_{sfc}$). Distributions are stratified according to wind speed (columns) and

precipitation (rows). Significant reductions in SFMR overestimates are found for the weaker wind cases ($U_{sfc} < 33$ m s$^{-1}$), both outside of rain (Fig. 12a, decrease from +2.4 to −0.2 m s$^{-1}$) and within rain (Fig. 12c, from +2.8 to +1.0 m s$^{-1}$), on average. Above the hurricane wind speed threshold (Figs. 12b,d), no significant changes in bias are found, and the mean biases for both the operational and revised algorithms are not significantly different from zero.

In Fig. 13, frequency distributions of SFMR wind speed bias are shown for measurements obtained in heavy precipitation ($R_{sfmr} > 20$ mm h$^{-1}$). As pictured in Fig. 13a, a significant reduction in mean bias from +5.1 to +3.7 m s$^{-1}$ for wind speeds less than hurricane force is found by applying the revised algorithm, although a high bias still remains. As for all rain conditions for wind speeds greater than hurricane force, no statistically significant biases are found in either the operational or revised algorithm retrievals (Fig. 13b).

Finally, wind speed retrieval accuracy is evaluated at the defined minimum criteria for tropical depressions (peak $U_{sfc} = 13$ m s$^{-1}$), tropical storms (peak $U_{sfc} = 18$ m s$^{-1}$), and hurricanes (peak $U_{sfc} = 33$ m s$^{-1}$). Surface wind speeds within ±4 m s$^{-1}$ of these thresholds are considered,
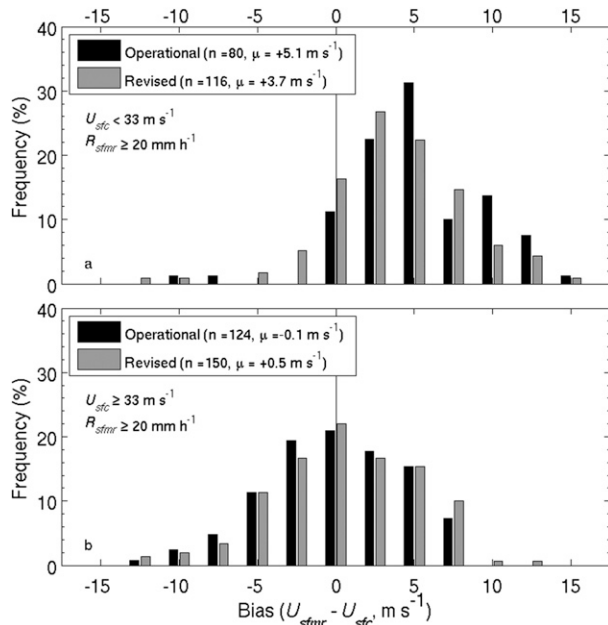
FIG. 13. As in Fig. 12, but for $R_{sfmr} > 20$ mm h$^{-1}$ when surface wind speed is (a) less than and (b) greater than the hurricane wind speed threshold.

since this value is approximately the uncertainty of SFMR winds according to the RMSE of the GMF. The wind speed bias as a function of SFMR rain rate for these three conditions for the operational and revised versions is shown in Fig. 14. Bin-average wind speed biases and corresponding 95% confidence intervals are computed. Note that bins for operational and revised rain rates are different, since the distribution of computed rain rates is different for each dataset (see Fig. 10).

For wind speeds around minimal depression (Fig. 14a) and tropical storm (Fig. 14b) strengths, there is a consistent reduction in the bias at all rain rates, but the significance in reduction at SFMR rain rates $> 20$ mm h$^{-1}$ may be lower because of limited sample sizes. For wind speeds near the hurricane wind speed threshold (Fig. 14c), no significant differences among versions are found, and the bias is less than $\sim 2$ m s$^{-1}$ over all retrieved rain rates. For wind speeds of $U_{sfc} \geq 40$ m s$^{-1}$, no bias is found to exist regardless of the rain rate (not shown).

## 6. Summary and conclusions

The operational SFMRs flown on the NOAA WP-3D and AFRC WC-130J fleet of aircraft provide surface wind speed measurements in the TC inner core and, when available, can aid forecasters in more accurately determining the intensity of a TC. Because the SFMR surface wind speed algorithm was developed primarily within hurricane conditions, the current algorithm is
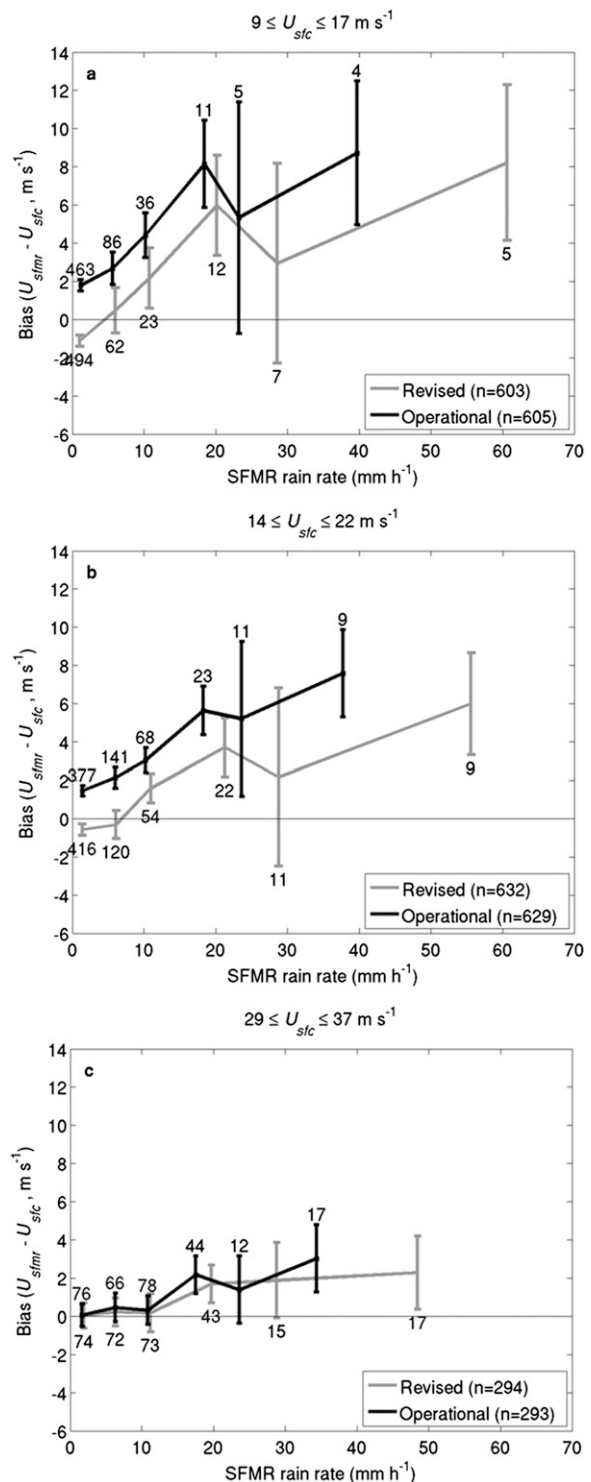


FIG. 14. Bin-averaged wind speed bias ($U_{sfmr} - U_{sfc}$, m s$^{-1}$) as a function of SFMR-retrieved rain rate for the operational (black) and revised (gray) SFMR wind speeds around the surface wind speed criteria for (a) tropical depression ($U_{sfc} = 13 \pm 4$ m s$^{-1}$), (b) tropical storm ($U_{sfc} = 18 \pm 4$ m s$^{-1}$), and (c) hurricane ($U_{sfc} = 33 \pm 4$ m s$^{-1}$). Error bars are 95% confidence intervals on bin average; numbers are bin counts. Note that rain-rate bins are defined separately for the operational and revised bias due to the extended range of retrieved rain rates using the revised model (see Fig. 10).

somewhat deficient at accurately measuring the surface wind speed in weak wind speed conditions, especially in heavy rain. Specifically, a significant high bias was quantified within all conditions as well as within weak wind speeds and heavy precipitation. The reason for this overestimation of weak wind speeds has been determined to be at least partly due to misrepresentation of microwave absorption by rain. To address this issue, a revised set of GMF coefficients for both the rain absorption and wind-induced surface emissivity models has been determined.

An evaluation of revised SFMR wind speed retrievals indicates that the bias is significantly reduced at wind speeds less than hurricane force ($U_{sfc} < 33\,\mathrm{m\,s^{-1}}$), and little difference is found at higher wind speeds where no significant bias initially existed. Additionally, SFMR-retrieved rain rates are more consistent with other instrument-derived rain-rate values. In cases where maximum rain rates in hurricanes did not exceed $\sim 60\,\mathrm{mm\,h^{-1}}$ with the currently operational version, the highest reported rain rates may now be as high as $\sim 90\,\mathrm{mm\,h^{-1}}$.

The proposed SFMR algorithm modifications are summarized as follows:

- *Sea surface emissivity:* The wind-induced excess emissivity at the 4.74-GHz channel is computed from Eq. (5) using the coefficients in Table 2. The excess emissivity for the additional channels are computed by applying the small frequency dependence from Eq. (6), multiplied by the frequency difference $\Delta f = f - 4.74\,\mathrm{GHz}$. Finally, the total surface emissivity is computed by Eq. (7) by adding the specular emissivity computed by the Klein and Swift (1977) algorithm.
- *Rain column depth:* As an improvement to simply assuming a constant height for the freezing level (4 km), the freezing level is computed from the observed flight-level temperature and altitude using Eq. (8).
- *Rain absorption coefficient:* The absorption coefficient is computed using previous methodology but uses the set of modified coefficients given in Table 3.

Although the surface wind speed overestimation by SFMR has evidently been significantly reduced in heavy rain using the revised model, a smaller high bias remains at the weakest wind speeds of tropical storm force and lower. The reasons for this bias are currently not clear, but further study is planned. Accordingly, the authors recommend applying a real-time bias adjustment based on the results depicted in Fig. 14, such that reported surface wind measurements are the statistically corrected values.

## REFERENCES

Aberson, S. D., M. L. Black, R. A. Black, J. J. Cione, C. W. Landsea, F. D. Marks, and R. W. Burpee, 2006: Thirty years of tropical cyclone research with the NOAA P-3 aircraft. *Bull. Amer. Meteor. Soc.,* **87,** 1039–1055, doi:10.1175/BAMS-87-8-1039.

Atlas, D., and C. W. Ulbrich, 1977: Path- and area-integrated rainfall measurement by microwave attenuation in the 1-3 cm band. *J. Appl. Meteor.,* **16,** 1322–1331, doi:10.1175/1520-0450(1977)016<1322:PAAIRM>2.0.CO;2.

Black, R. A., and J. Hallet, 2012: Rain rate and water content in hurricanes compared with summer rain in Miami, FL. *J. Appl. Meteor. Climatol.,* **51,** 2218–2235, doi:10.1175/JAMC-D-11-0144.1.

D'Asaro, E. A., and Coauthors, 2014: Impact of typhoons on the ocean in the Pacific: ITOP. *Bull. Amer. Meteor. Soc.,* doi:10.1175/BAMS-D-12-00104.1, in press.

Dunion, J. P., C. W. Landsea, S. H. Houston, and M. D. Powell, 2003: A reanalysis of the surface winds for Hurricane Donna of 1960. *Mon. Wea. Rev.,* **131,** 1992–2011, doi:10.1175/1520-0493(2003)131<1992:AROTSW>2.0.CO;2.

Franklin, J. L., M. L. Black, and K. Valde, 2003: GPS dropwindsonde wind profiles in hurricanes and their operational implications. *Wea. Forecasting,* **18,** 32–44, doi:10.1175/1520-0434(2003)018<0032:GDWPIH>2.0.CO;2.

Gamache, J. F., F. D. Marks, and F. Roux, 1995: Comparison of three airborne Doppler sampling techniques with airborne in situ wind observations in Hurricane Gustav (1990). *J. Atmos. Oceanic Technol.,* **12,** 171–181, doi:10.1175/1520-0426(1995)012<0171:COTADS>2.0.CO;2.

Gray, W. M., C. Neumann, and T. L. Tsui, 1991: Assessment of the role of aircraft reconnaissance on tropical cyclone analysis and forecasting. *Bull. Amer. Meteor. Soc.,* **72,** 1867–1883, doi:10.1175/1520-0477(1991)072<1867:AOTROA>2.0.CO;2.

Hock, T. F., and J. L. Franklin, 1999: The NCAR GPS dropwindsonde. *Bull. Amer. Meteor. Soc.,* **80,** 407–420, doi:10.1175/1520-0477(1999)080<0407:TNGD>2.0.CO;2.

Jiang, H., P. G. Black, E. J. Zipser, F. D. Marks, and E. W. Uhlhorn, 2006: Validation of rain-rate estimation in hurricanes from the Stepped Frequency Microwave Radiometer: Algorithm correction and error analysis. *J. Atmos. Sci.,* **63,** 252–267, doi:10.1175/JAS3605.1.

——, E. M. Ramirez, and D. J. Cecil, 2013: Convective and rainfall properties of tropical cyclone inner cores and rainbands from 11 years of TRMM data. *Mon. Wea. Rev.,* **141,** 431–450, doi:10.1175/MWR-D-11-00360.1.

Jorgensen, D. P., 1984: Mesoscale and convective-scale characteristics of mature hurricanes. Part I: General observations by research aircraft. *J. Atmos. Sci.,* **41,** 1268–1286, doi:10.1175/1520-0469(1984)041<1268:MACSCO>2.0.CO;2.

——, and P. L. Willis, 1982: A *Z–R* relationship for hurricanes. *J. Appl. Meteor.,* **21,** 356–366, doi:10.1175/1520-0450(1982)021<0356:AZRRFH>2.0.CO;2.

——, P. H. Hildebrand, and C. L. Frush, 1983: Feasibility test of an airborne pulse-Doppler meteorological radar. *J. Climate Appl. Meteor.,* **22,** 744–757, doi:10.1175/1520-0450(1983)022<0744:FTOAAP>2.0.CO;2.

Klein, L. A., and C. T. Swift, 1977: An improved model for the dielectric constant of sea water at microwave frequencies. *IEEE Trans. Antennas Propag.,* **2,** 104–111, doi:10.1109/JOE.1977.1145319.

Lorsolo, S., J. A. Zhang, F. Marks, and J. Gamache, 2010: Estimation and mapping of hurricane turbulent energy using airborne Doppler measurements. *Mon. Wea. Rev.,* **138,** 3656–3670, doi:10.1175/2010MWR3183.1.

Marks, F. D., 1985: Evolution of the structure of precipitation in Hurricane Allen (1980). *Mon. Wea. Rev.,* **113,** 909–930, doi:10.1175/1520-0493(1985)113<0909:EOTSOP>2.0.CO;2.

——, R. A. Houze, and J. F. Gamache, 1992: Dual-aircraft investigation of the inner core of Hurricane Norbert. Part I: Kinematic structure. *J. Atmos. Sci.,* **49,** 919–942, doi:10.1175/1520-0469(1992)049<0919:DAIOTI>2.0.CO;2.

Matrosov, S., K. A. Clark, B. E. Martner, and A. Tokay, 2002: X-band polarimetric radar measurements of rainfall. *J. Appl. Meteor.,* **41,** 941–952, doi:10.1175/1520-0450(2002)041<0941:XBPRMO>2.0.CO;2.

——, D. E. Kingsmill, B. E. Martner, and F. M. Ralph, 2005: The utility of X-band polarimetric radar for quantitative estimates of rainfall parameters. *J. Hydrometeor.,* **6,** 248–262, doi:10.1175/JHM424.1.

Monahan, E. C., 1971: Oceanic whitecaps. *J. Phys. Oceanogr.,* **1,** 139–144, doi:10.1175/1520-0485(1971)001<0139:OW>2.0.CO;2.

Nordberg, W. J., J. Conaway, D. B. Ross, and T. Wilheit, 1971: Measurements of microwave emission from a foam-covered, wind-driven sea. *J. Atmos. Sci.,* **28,** 429–435, doi:10.1175/1520-0469(1971)028<0429:MOMEFA>2.0.CO;2.

Olsen, R., D. V. Rogers, and D. B. Hodge, 1978: The $aR^b$ relation in calculation of rain attenuation. *IEEE Trans. Antennas Propag.,* **26,** 318–329, doi:10.1109/TAP.1978.1141845.

Park, S.-G., V. N. Bringi, V. Chandrasekar, M. Maki, and K. Iwanami, 2005: Correction of radar reflectivity and differential reflectivity for rain attenuation at X band. Part I: Theoretical and empirical basis. *J. Atmos. Oceanic Technol.,* **22,** 1621–1632, doi:10.1175/JTECH1803.1.

Powell, M. D., P. P. Dodge, and M. L. Black, 1991: The landfall of Hurricane Hugo in the Carolinas: Surface wind distribution. *Wea. Forecasting,* **6,** 379–399, doi:10.1175/1520-0434(1991)006<0379:TLOHHI>2.0.CO;2.

Ralph, F. M., and Coauthors, 2013: The emergence of weather-related test beds linking research and forecasting operations. *Bull. Amer. Meteor. Soc.,* **94,** 1187–1211, doi:10.1175/BAMS-D-12-00080.1.

Rappaport, E. N., J.-G. Jiing, C. W. Landsea, S. T. Murillo, and J. L. Franklin, 2012: The Joint Hurricane Test Bed: Its first decade of tropical cyclone research-to-operations activities reviewed. *Bull. Amer. Meteor. Soc.,* **93,** 371–380, doi:10.1175/BAMS-D-11-00037.1.

Rinehart, R. E., 2004: *Radar for Meteorologists.* 4th ed. Rinehart Publications, 482 pp.

Rogers, R., and Coauthors, 2006: The Intensity Forecasting Experiment: A NOAA multiyear field program for improving tropical cyclone intensity forecasts. *Bull. Amer. Meteor. Soc.,* **87,** 1523–1537, doi:10.1175/BAMS-87-11-1523.

——, and Coauthors, 2013: NOAA's Hurricane Intensity Forecasting Experiment (IFEX): A progress report. *Bull. Amer. Meteor. Soc.,* **94,** 859–882, doi:10.1175/BAMS-D-12-00089.1.

Rosenfeld, D., D. B. Wolff, and D. Atlas, 1993: General probability-matched relations between radar reflectivity and rain rate. *J. Appl. Meteor.,* **32,** 50–72, doi:10.1175/1520-0450(1993)032<0050:GPMRBR>2.0.CO;2.

——, ——, ——, and E. Amitai, 1994: The window probability matching method for rainfall measurements with radar. *J. Appl. Meteor.,* **33,** 682–693, doi:10.1175/1520-0450(1994)033<0682:TWPMMF>2.0.CO;2.

Rosenkranz, P. W., and D. H. Staelin, 1972: Microwave emissivity of ocean foam and its effect on nadiral radiometric measurements. *J. Geophys. Res.,* **77,** 6528–6538, doi:10.1029/JC077i033p06528.

Ross, D. B., and V. Cardone, 1974: Observations of oceanic whitecaps and their relation to remote measurements of surface wind speed. *J. Geophys. Res.,* **79,** 444–452, doi:10.1029/JC079i003p00444.

Smith, E. K., 1982: Centimeter and millimeter wave attenuation and brightness temperature due to atmospheric oxygen and water vapor. *Radio Sci.,* **17,** 1455–1464, doi:10.1029/RS017i006p01455.

Swift, C. T., D. C. DeHority, P. G. Black, and J.-Z. Chein, 1984: Microwave remote sensing of ocean surface wind speed and rain rates over tropical storms. *Frontiers of Remote Sensing of the Oceans and Troposphere from Air and Space Platforms: Proceedings of the URSI Commission F Symposium and Workshop,* NASA Conference Publication, Vol. 2303, NASA, 281–286.

Tanner, A. C., C. T. Swift, and P. G. Black, 1987: Operational airborne remote sensing of wind speeds in hurricanes. Preprints, *17th Conf. on Hurricanes and Tropical Meteorology,* Miami, FL, Amer. Meteor. Soc., 385–387.

Tsang, L., J. A. Kong, E. Njoku, D. H. Staelin, and J. W. Waters, 1977: Theory for microwave thermal emission from a layer of cloud or rain. *IEEE Trans. Antennas Propag.,* **25,** 650–657, doi:10.1109/TAP.1977.1141664.

Uhlhorn, E. W., and P. G. Black, 2003: Verification of remotely sensed sea surface winds in hurricanes. *J. Atmos. Oceanic Technol.,* **20,** 99–116, doi:10.1175/1520-0426(2003)020<0099:VORSSS>2.0.CO;2.

——, and D. S. Nolan, 2012: Observational undersampling in tropical cyclones and implications for estimated intensity. *Mon. Wea. Rev.,* **140,** 825–840, doi:10.1175/MWR-D-11-00073.1.

——, P. G. Black, J. L. Franklin, M. Goodberlet, J. Carswell, and A. S. Goldstein, 2007: Hurricane surface wind measurements from an operational Stepped Frequency Microwave Radiometer. *Mon. Wea. Rev.,* **135,** 3070–3085, doi:10.1175/MWR3454.1.

——, B. W. Klotz, T. Vukicevic, P. D. Reasor, and R. F. Rogers, 2014: Observed hurricane wind speed asymmetries and relationships to motion and environmental shear. *Mon. Wea. Rev.,* **142,** 1290–1311, doi:10.1175/MWR-D-13-00249.1.

Walsh, E. J., I. PopStefanija, S. Y. Matrosov, J. Zhang, E. Uhlhorn, and B. Klotz, 2014: Airborne rain-rate measurement with a wide-swath radar altimeter. *J. Atmos. Oceanic Technol.,* **31,** 860–875, doi:10.1175/JTECH-D-13-00111.1.

Webster, W. J., Jr., T. T. Wilheit, D. B. Ross, and P. Gloersen, 1976: Spectral characteristics of the microwave emission from a wind-driven foam-covered sea. *J. Geophys. Res.,* **81,** 3095–3099, doi:10.1029/JC081i018p03095.

Zhang, J. A., and E. W. Uhlhorn, 2012: Hurricane sea surface inflow angle and observation-based parametric model. *Mon. Wea. Rev.,* **140,** 3587–3605, doi:10.1175/MWR-D-11-00339.1.